

Plasma-chemical processes in microwave plasma-enhanced chemical vapor deposition reactors operating with C/H/Ar gas mixtures

Yuri A. Mankelevich,^{1,a)} Michael N. R. Ashfold,² and Jie Ma²

¹*Skobel'tsyn Institute of Nuclear Physics, Moscow State University, Vorob'evy gory, Moscow 119991, Russia*

²*School of Chemistry, University of Bristol, Bristol BS8 1TS, United Kingdom*

(Received 31 July 2008; accepted 18 October 2008; published online 10 December 2008)

Microwave (MW) plasma-enhanced chemical vapor deposition (PECVD) reactors are widely used for growing diamond films with grain sizes spanning the range from nanometers through microns to millimeters. This paper presents a detailed description of a two-dimensional model of the plasma-chemical activation, transport, and deposition processes occurring in MW activated H/C/Ar mixtures, focusing particularly on the following base conditions: 4.4%CH₄/7%Ar/balance H₂, pressure $p=150$ Torr, and input power $P=1.5$ kW. The model results are verified and compared with a range of complementary experimental data in the companion papers. These comparators include measured (by cavity ring down spectroscopy) C₂(a), CH(X), and H($n=2$) column densities and C₂(a) rotational temperatures, and infrared (quantum cascade laser) measurements of C₂H₂ and CH₄ column densities under a wide range of process conditions. The model allows identification of spatially distinct regions within the reactor that support net CH₄→C₂H₂ and C₂H₂→CH₄ conversions, and provide a detailed mechanistic picture of the plasma-chemical transformations occurring both in the hot plasma and in the outer regions. Semianalytical expressions for estimating relative concentrations of the various C₁H _{x} species under typical MW PECVD conditions are presented, which support the consensus view regarding the dominant role of CH₃ radicals in diamond growth under such conditions. © 2008 American Institute of Physics.

[DOI: [10.1063/1.3035850](https://doi.org/10.1063/1.3035850)]

I. INTRODUCTION

Diamond films can be deposited in microwave (MW) plasma-enhanced chemical vapor deposition (PECVD) reactors with a range of grain sizes—ranging from nanometers through microns to millimeters (single crystal material) depending upon the choice of gas mixture, growth conditions, substrate properties, and growth time. Typical deposition conditions involve use of a gas mixture containing a small quantity of a hydrocarbon (e.g., a few percent CH₄ in excess hydrogen), input powers $P\sim 1$ kW, and gas pressures $p\sim 100\text{--}200$ Torr.¹ The main growth species involved in microcrystalline diamond (MCD) deposition is generally accepted to be the CH₃ radical, which adds to a radical site on the diamond surface formed by H abstraction from a surface C–H bond by an incident gas phase H atom.^{2,3} In argon rich mixtures (e.g., 1%CH₄/2%H₂/97%Ar), the grain size of the films decreases and eventually becomes on the order of nanometers.⁴ Such nanocrystalline diamond (NCD) and ultrananocrystalline diamond (UNCD) films are much smoother than a microcrystalline film. Early studies suggested the C₂ radical as the main growth species for (U)NCD films,⁴ but more recent two-dimensional (2D) model calculations suggest that the most probable UNCD precursors are more likely to be C atoms under MW PECVD conditions^{5,6} and CH₃ radicals in hot filament (HF) CVD reactors.^{6,7} Related 2D model calculations⁸ suggest that CH₃ radicals are

the predominant growth species for single crystal diamond (SCD) formed under high power density MW PECVD conditions using a 10%CH₄/H₂ mixture.⁹

Many complex and interrelated phenomena need to be considered when simulating the full range of diamond deposition conditions and processes occurring in a MW PECVD reactor. These include the propagation of the electromagnetic fields (E, H) in the reactor chamber; the spatial distribution of these fields and their interaction with the plasma; gas heating; heat and mass transfer; a plethora of (charged and neutral) species and the huge array of plasma-chemical reactions for real feed gases (i.e., H/C or H/C/noble gas mixtures); the nonequilibrium electron energy distribution; radiation processes; species diffusion and thermodiffusion; and the loss and conversion of charged and neutral species at the surface of the substrate, substrate holder, and the reactor walls. Ideally, all of these processes should be accommodated in a self-consistent manner, using (at least) a 2D coordinate system, e.g., (r, z) in the case of a reactor with cylindrical symmetry. To realize such an approach is a problem of extreme complexity, however, that would require an enormous amount of computational time. Thus, various simplifications have been used in all such models developed over the past decade—e.g., 2D models including realistic treatment of the electromagnetic field but restricted to the case of pure H₂,^{10–14} 2D models for H/C mixtures⁸ and for H/C/Ar (Refs. 5 and 6) mixtures but without explicit calculation of the (E, H) fields, and various one-dimensional models (in the axial z and radial r directions) for H/C (Ref. 15) and H/C/Ar (Ref. 16) mixtures.

^{a)}Author to whom correspondence should be addressed. Electronic mail: ymankelevich@mics.msu.su.

In previous studies, we have applied our 2D model of MW PECVD reactors to the simulation of both SCD (Refs. 6 and 8) and UNCD growth conditions.^{5,6} Here and in three companion papers (Refs. 17–19), we describe the results of a series of experimental and theoretical studies of the processes prevailing in a MW PECVD reactor operating under typical conditions for MCD deposition from H/C/Ar (H/C/Ne) gas mixtures at $p=75\text{--}150$ Torr and $P=1\text{--}1.5$ kW. The model has been tested thoroughly, against a large body of (spatially resolved) experimental data obtained via systematic variation of a range of reactor parameters including total pressure p , input power P , carbon source gas and its partial pressure, and the partial pressure of added noble gas (argon or neon).

II. 2D MODEL

A 2D (r, z) model is used to describe essential processes occurring in a MW PECVD reactor and to provide spatial distributions of the gas temperature T and species concentrations, growth rates, power absorption, and transfer channels as functions of reactor operating conditions. Cylindrical symmetry is assumed, so the two important coordinates are r , the radial distance from the centerline of the chamber, and z , the axial (vertical) height above the substrate surface. The rate coefficients of the various plasma activation reactions (electron-atom and electron-molecule reactions) depend on the local electron energy distribution function (EEDF). The EEDF in an oscillating electric field $E \sin(\omega t)$ is a function of the ratio $E/(\omega^2 + \nu_m^2)^{0.5}$,²⁰ where $\omega = 2\pi f$, $f = 2.45 \times 10^9$ Hz is the MW discharge frequency, and ν_m is an effective collision frequency. This collision frequency ν_m (which scales with the gas number density N) far exceeds the exciting field frequency ($\nu_m \gg \omega$) at the pressures ($p \sim 75\text{--}150$ Torr) and gas concentrations of interest in the present work, and the local EEDF is thus a function of reduced electric field E/N .²⁰ However, the present 2D model for real H/C/Ar gas mixtures does not include explicit calculation of the electromagnetic fields. Rather, it involves the following two simplifying assumptions.

First, the steep exponential dependence of the ionization rates and electron density on the reduced electric field E/N ensures that only a narrow range of E/N values will be realized in a MW discharge plasma excited by any given input power density. Support for this statement is provided by our previous self-consistent calculations of electromagnetic fields and plasma parameters for pure hydrogen plasma,^{10,12} which show that E/N and the average electron temperature T_e both tend to be distributed uniformly throughout the whole plasma region except at the plasma edge (the boundary shell). Similar findings (i.e., only $\sim 10\%$ decline in T_e with increasing distance from the substrate) have been reported for self-consistent 2D calculations of pure H_2 at $p = 83$ Torr and $P = 2$ kW.¹¹ Second, the size of the plasma region used in the model (i.e., radius R_{pl} and height H_{pl} in the case of a cylindrical plasma volume) is an external parameter, guided by experimental absorption and/or optical emission spectroscopy data.

As shown below, these simplifications allow the MW

power absorption and activation volume to be accommodated as parameters within the model blocks and thus estimation of E/N and T_e in the plasma region for a given value of input power. The main model blocks are incorporated in a self-consistent manner and describe

- (i) power absorption and gas heating, heat, and mass transfer;
- (ii) plasma activation of the reactive gas mixture, the plasma-chemical kinetics involving nonequilibrium EEDF calculations, and species diffusion and thermal diffusion; and
- (iii) gas-surface processes (diamond deposition and loss/production of radicals, ions, and electrons).

The set of nonstationary conservation equations for mass, momentum, energy [block (i), Eqs. (1)–(4)], and species concentrations [blocks (ii) and (iii), Eqs. (5)–(7)] are solved numerically by a finite difference method in (r, z) coordinates,

$$\nabla_r \rho = -\nabla(\rho \vec{v}), \quad (1)$$

$$\nabla_r(\rho u) = -\nabla(\rho u \vec{v}) - \nabla_r p + \nabla W_z, \quad (2)$$

$$\nabla_r(\rho v) = -\nabla(\rho v \vec{v}) - \nabla_r p + \nabla W_r + \frac{2}{3r} \left\{ \mu \frac{\partial u}{\partial r} - v \left(\frac{2\mu}{r} + \frac{\partial \mu}{\partial r} \right) \right\}, \quad (3)$$

$$\nabla_r(\rho \varepsilon) = -\nabla(\rho \varepsilon \vec{v}) - p \nabla_z u - \left(\frac{p}{r} \right) \nabla_r(rv) - \nabla Q_\lambda - \nabla \left(\sum_{i=1}^k h_i j_i \right) + Q_J + W_\varepsilon, \quad (4)$$

$$\nabla_r n_i = -\nabla(n_i \vec{v} + j_i/m_i) + S_i - L_i n_i, \quad (5)$$

where $\nabla_x = \partial/\partial x$, $x = t, z, r$, $\nabla(\rho \vec{v}) = \partial(\rho u)/\partial z + \partial(r\rho v)/r \partial r$, ρ is the gas density, $\vec{v} = (u, v)^T$, u and v are the axial and radial flow velocity components, and p is a scalar pressure. The viscosity terms²¹ are given by

$$W_z = \left(2\mu \nabla_z u - \frac{2}{3} \mu \nabla \vec{v}, \mu(\nabla_r u + \nabla_z v) \right)^T,$$

$$W_r = \left(\mu(\nabla_r u + \nabla_z v), 2\mu \nabla_r v - \frac{2}{3} \mu \nabla \vec{v} \right)^T,$$

$$W_\varepsilon = \mu \left[\frac{4}{3} (\nabla_z u)^2 + \frac{4}{3} \left(\frac{\nabla_r(rv)}{r} \right)^2 + (\nabla_z u + \nabla_r v)^2 - \frac{2}{r} \nabla_r v^2 - \frac{4}{3} (\nabla_z u) \frac{\nabla_r(rv)}{r} \right].$$

$\mu = \mu(T)$ is the gas viscosity, ε and h are the specific energy and enthalpy, respectively, $Q_\lambda = (-\lambda \nabla_z T, -\lambda \nabla_r T)^T$, $\lambda = \lambda(T)$ is a thermal conductivity, and T is the gas temperature. Q_J is the gas heating source as a result of MW power absorption by electrons, further energy transfer to (excited states of) gas phase particles, and their subsequent collisional deactivation.

n_i and m_i are the concentration and mass of species i , respectively. The mass diffusion flux of the i th species is treated as a diffusion of a low fraction component in a triple mixture comprising two base components, Ar and H₂ [i.e., in terms of mole fractions ($X_i = n_i/N$), $X_i \ll X_{H_2} + X_{Ar}$]. In this case, the diffusional and thermodiffusional fluxes of the i th species can be approximated²² as

$$j_i = -m_i D_i N \nabla X_i - D_i^T \nabla T/T, \quad (6)$$

where $D_i = D_{i,H_2}/[1 + X_{Ar}\{(D_{i,H_2}/D_{i,Ar}) - 1\}]$ and $D_{i,k}$ (cm² s⁻¹) and D_i^T (g cm⁻¹ s⁻¹) are the species dependent binary molecular diffusivity and thermal diffusion coefficients, respectively. $D_i \approx D_{i,H_2}$ for low argon mole fractions (i.e., $X_{Ar} < 0.2$). The binary diffusion and thermodiffusion coefficients were calculated from Lennard–Jones parameters²³ and D_i for the various neutral species were approximated as $D_i = a_i T^{1.7}/p$.²⁴ Characteristic values of the factors a for H atoms, CH₃ radicals, and C₂H₂ molecules in a 7%Ar/H₂ mixture are as follows: $a_H = 0.103$, $a_{CH_3} = 0.0314$, and $a_{C_2H_2} = 0.0264$ for D_i in cm² s⁻¹, T in K, and p in Torr.

The bulk plasma in a high-pressure discharge such as the present case is quasineutral, $|n_e - \sum n_{+i}| \ll n_e \approx \sum n_{+i}$, and we assume ambipolar transport of the charged species; i.e., the charged species cannot be separated and their transport is treated as a diffusion with a common (ambipolar) diffusion coefficient $D_a \approx D_{ion}(1 + T_e/T_{ion})$.²⁰ Here, n_e and T_e are the electron concentration and temperature, respectively. The ion temperature T_{ion} under our discharge conditions is close to the gas temperature (i.e., $T_{ion} \approx T$), and D_{ion} is the average ion diffusion coefficient $D_{ion} \approx \sum D_{+i} \nabla n_{+i} / \nabla n_e$. In situations where there is one predominant ion (with diffusion coefficient D_+), or in cases where there are several ionic species with similar diffusion coefficients $D_{+i} \approx D_+$, the average diffusion coefficient D_{ion} can be expressed²⁰ as $D_{ion} \approx D_+ \approx \mu_+ (\text{cm}^2 \text{V}^{-1} \text{s}^{-1}) N T_{ion} (\text{eV}) / N = a_+ T^2 / p$. In reaching this expression, we have assumed that the ion mobilities satisfy the condition $\mu_+ N \approx \text{const}$ and the ideal gas equation of state $p = NkT$. This leads to the ambipolar diffusion coefficient D_a having the following T_e and T dependence: $D_a \approx a_+ T(T + T_e) / p$. The present calculations employ the value $a_+ = 0.00285$ for the H₃⁺ ions that dominate in the Ar/H₂ plasma and $a_+ = 0.002$ for the C₂H₂⁺ and C₂H₃⁺ ions that are most abundant in H/C/Ar plasmas with, as before, D_i in cm² s⁻¹, T in K, and p in Torr.

The terms S_i and $L_i n_i$ in Eq. (5) represent the respective production and loss rates of chemical species i . The plasma-chemical reaction mechanism was processed using the chemical translator developed as part of the modeling routine. For each species, this translator automatically generates the loss/production terms needed for numerical solution of the chemical kinetic mechanism. The inverse reaction rate constants were also computed by the chemical translator using documented thermochemical data.²⁵

The gas phase plasma chemistry and thermochemical input for H/C/Ar mixtures are taken from a range of sources. These include the detailed reaction mechanism for neutral C_xH_y species,^{25,26} plasma-chemical reactions,^{15,26} collision processes in a hydrogen plasma, along with cross sections for e -H and e -H₂ collisions^{27–33} and e -C_xH_y cross

sections.^{34,35} The plasma-chemical kinetics mechanism includes more than 240 direct and reverse reactions for 30 neutral species [C, CH, CH₂(X) (henceforth ³CH₂), CH₂(a) [henceforth ¹CH₂ or CH₂(s)], CH₃, CH₄, C₂(X), C₂(a), C₂H, C₂H₂, C₂H₃, C₂H₄, C₂H₅, C₂H₆, C₃, C₃H, C₃H₂, C₄, C₄H, C₄H₂, H, H₂ ($v=0, 1, 2$), electronically excited H($n=2$) and H($n=3$) atoms, metastable (Ar*) and resonance (Ar**) states of Ar (treated as “effective” states with the energies of the lowest such states, i.e., the states with configuration $3p^5 4s^1$ at 11.54 and 11.72 eV for Ar* and 11.62 and 11.82 eV for Ar**), an effective state representing electronically excited H₂ (H₂*), and eight charged species (electrons and the ions C₂H₂⁺, C₂H₃⁺, H⁺, H₂⁺, H₃⁺, Ar⁺, and ArH⁺). The plasma-chemical kinetics mechanism was further extended when modeling the gas phase chemistry prevailing in UNCD deposition conditions [i.e., (0.5%–1%)CH₄/(0%–2%)H₂ in excess Ar] by the inclusion of additional ions (C⁺, C₂⁺, C₃⁺, CH⁺, C₂H⁺, and C₃H⁺).^{5,6} No negative ions are included in the present calculations; tests of an extended plasma-chemical mechanism that includes production and loss processes for the H⁻ negative ion show its concentration to be too low to be of importance in MW PECVD reactors.

Modeling the electron-molecule (atom) reaction coefficients, as well as their dependence on the local EEDF and the reduced electric field E/N , requires special consideration. These quantities have been estimated using a zero-dimensional framework, wherein the local balance equations of plasma-chemical kinetics for charged and neutral species are solved for the range of E/N and T_{gas} values of interest. The EEDF [$n(\epsilon)$] is calculated simultaneously with the composition of the H/C/Ar gas mixture by solving the Boltzmann equation using a two-term approximation.²⁰

$$\frac{dn}{dt} = \frac{\partial}{\partial \epsilon} \left(D_\epsilon \frac{\partial n}{\partial \epsilon} + C_\epsilon n \right) + I_c, \quad (7)$$

where

$$D_\epsilon = \frac{2e^2 E^2}{3m_e \sum_i X_i \nu_{mi}} \epsilon,$$

and

$$C_\epsilon = \sum_i \frac{2m_e}{m_i} \epsilon \nu_{mi} - \frac{e^2 E}{3m_e \sum_i X_i \nu_{mi}}.$$

$n(\epsilon)$ in Eq. (7) is normalized such that $\int n(\epsilon) d\epsilon = n_e$, and m_e and m_i are the electron mass and the mass of particle i , respectively. The appropriate elastic cross sections σ_{mi} for the various electron-particle collisions, together with the relation

$$\nu_{mi}(\epsilon) = \sigma_{mi}(\epsilon) (2\epsilon/m_e)^{0.5} n_i,$$

are used to calculate the electron energy (ϵ) dependence of the coefficients D_ϵ and C_ϵ . Calculation of the inelastic collision integral I_c (Ref. 36) employs cross sections σ_j for a range of relevant processes j including excitation/deexcitation of rotational (R) and vibrational (V) states, electronic state excitations, and ionization of the various species in the gas mixture. As a result, the rate coefficients k_j

$=\langle\sigma_j(\varepsilon)(2\varepsilon/m_e)^{0.5}\rangle$ of electron-dependent reactions are obtained as functions of E/N (or T_e) and gas temperature T for use in the 2D model. Use of different T_e values allows simulation of the effects of different power densities and plasma volumes (while retaining a given total input power).

The absorbed power density Q_J (in W cm^{-3}) as a function of E/N , gas temperature T , and electron density n_e can be estimated in a local equilibrium approach as follows:

$$Q_J \sim jE \sim en_e\mu_e N \left(\frac{E}{N}\right) E = e(\mu_e N) \left(\frac{E}{N}\right)^2 n_e \left(\frac{p}{kT}\right) \approx C(p, E/N) \frac{n_e}{T}. \quad (8)$$

e , j , and μ_e in Eq. (8) are the electron charge, current density, and mobility, respectively, and k is the Boltzmann constant. $C(p, E/N)$ only varies weakly within the plasma volume and the T^{-1} dependence of Q_J is the factor of primary importance in preventing the plasma ball from artificial overheating—as observed in our previous calculations.⁵

In the present 2D calculations, the absorbed power density Q_J is calculated directly as a sum of power losses and gains associated with the various electron-particle reactions (e.g., electronic, vibrational, and rotational excitation/deexcitation, dissociation, and ionization), i.e.,

$$Q_J = \sum_i k_i N_j n_e \varepsilon_i. \quad (9)$$

ε_i in Eq. (9) is the electron energy loss ($\varepsilon_i > 0$) or gain ($\varepsilon_i < 0$) accompanying the i th reaction. For the typical conditions prevailing in a MW PECVD reactor operating with $\text{C}_x\text{H}_y/\text{H}_2$ gas mixtures, the major fraction of the MW power absorbed by the electrons (>90%–95%) is used in vibrational and rotational excitation of gas phase molecules (H_2 and C_xH_y). The remainder is consumed by dissociation of H_2 and C_xH_y molecules, electronic excitation of atomic and molecular species, and ionization. Subsequent collisions between the excited neutral molecules and ground state molecules in the background gas lead to this excess energy becoming redistributed around the plasma ball, and cause it to heat to $T \sim 2900$ K. Thermal dissociation of molecular hydrogen becomes a major source of H atoms in a hydrogen plasma at high temperatures ($T \geq 2800$ K). These serve to initiate further production of the various hydrocarbon radical species necessary for diamond growth. A proper treatment of H_2 rotational and vibrational excitation (by electron impact) and deexcitation [by V-translational (T) relaxation by H atoms] processes is essential for obtaining a reliable prediction of T in a MW PECVD reactor operating under the typical conditions used for MCD and SCD growth.

The surface kinetics block (iii) accommodates the reactions of hydrocarbon species as well as atomic and molecular hydrogen with a solid (at the substrate and substrate holder) and recombination of atomic hydrogen at the chamber walls. Literature values for H atom sticking coefficients at a cold metal wall are as high as $\gamma_{\text{H}}=0.15$,³⁷ but the inner surfaces of most CVD reactors will be coated with some carbonaceous deposit—under which circumstances γ_{H} may well be one or two orders of magnitude lower.³⁸ We have assumed a base

value of $\gamma_{\text{H}}=0.001$. Calculations with the high γ_{H} value (0.15) show that the effect of this change on H atom (and hydrocarbon molecules) is confined to the near wall region. Gas-surface reactions within the diamond growth mechanism^{7,8} involve H abstraction to form monoradical and biradical surface sites. The subsequent reactions of these sites with H, H_2 , and hydrocarbon radicals serve to set boundary conditions for gas species and to alter the gas composition close to the surface. The main effect of these reactions is to reduce the H atom concentrations directly above the growing diamond surface and the surface of the substrate holder that, in turn, affects the hydrocarbon radical concentrations and can have major implications for subsequent growth.

The grid points closest to the substrate surface for which the model calculates species concentrations are located at a distance $0.5dz$, where dz is the grid cell size in the axial direction (i.e., perpendicular to the substrate surface) that, in the present calculations, was set to 1 mm. Near the surface, however, there is often a thin (<1 mm) boundary layer in which temperatures, gas flows, and concentrations can change significantly. The chemical composition in this thin boundary layer cannot be calculated accurately with a chemical mechanism employing temperature-dependent reaction rates and with assumed equilibrium thermal velocity and energy distributions based on a given local temperature. This thin boundary layer is therefore not included in the present 2D model. However, reliable estimates of the fluxes of the various species arriving at the substrate surface are required if we are to develop growth mechanisms and to calculate growth rates. These values have been estimated in different ways for H atoms, H_2 molecules, and hydrocarbon species.

H atoms. We have used an approach similar to that proposed by Dandy and Coltrin²³ to accommodate the substantial loss of H atoms at the substrate and substrate holder surfaces. This approach provides the relationship between H atom concentrations at the substrate, $[\text{H}]$, and near the substrate, $[\text{H}]_{\text{ns}}$, via

$$D_{\text{H}} N([\text{H}]_{\text{ns}}/[\text{N}]_{\text{ns}} - [\text{H}]/[\text{N}]) / (0.5dz) = \gamma(T_s, [\text{H}], [\text{H}_2]) V_{\text{H}}[\text{H}] / 4. \quad (10)$$

V_{H} in Eq. (1) is the H atom thermal velocity at the local temperature T_{gas} and the function $\gamma(T_s, \text{H}_s, \text{H}_2)$ is the H atom loss probability at substrate temperature T_s , which can be expressed as

$$\gamma(T_s, [\text{H}], [\text{H}_2]) = 0.83 / \{1 + 0.3 \exp(3430/T_s) + 0.1 \exp(-4420/T_s) [\text{H}_2]/[\text{H}]\}, \quad (11)$$

taking into account the reactions of H atom abstraction (direct and reverse) and addition.⁷

Buffer gas, H_2 , and Ar. The present 2D model calculations serve to emphasize that there can be a significant difference between the gas temperature near the substrate, T_{ns} , and the actual substrate temperature T_s (e.g., $T_s=973$ K, but $T_{\text{ns}} \sim 1300$ K at $0.5dz=0.5$ mm from the substrate). As a first approach, we have assumed $[\text{B}] \approx [\text{B}]_{\text{ns}} T_{\text{ns}}/T_s$ for $\text{B}=\text{H}_2$ and for Ar. This last condition implies that the mole fraction remains constant across the thin boundary layer,

which is likely to be valid for species with low reaction probabilities at the surface.

CH₃ and other hydrocarbons. [CH₃] at the surface is assumed to be approximately the same as the methyl concentration [CH₃]_{ns} calculated numerically at the grid point closest to the substrate, (i.e., at 0.5dz=0.5 mm). Similarly, for all other hydrocarbon species, we assume [C_mH_x] ≈ [C_mH_x]_{ns}. This approximation is justifiable for HF CVD reactors, in which there are generally no significant boundary layers (e.g., thermal and chemical) at the substrate surface. MW PECVD reactors are more complex, however, especially at higher powers. In these cases, a thin boundary layer could exist adjacent to the substrate surface in which the temperature may change by hundreds of kelvins over a length scale <1 mm. In the absence of a better model of this boundary region in MW systems, however, we have assumed that hydrocarbon species show the same near substrate behavior as in HF CVD systems.

Under the present base conditions (i.e., with T_s=973 K, with CH₃ as the dominant C₁ radical species), the previously proposed formula^{6,8} for growth rates G(μm/h) can be expressed as

$$G_{\text{CH}_3} = 3.8 \times 10^{-14} T_s^{0.5} [\text{CH}_3] R \{0.5 / (1 + 1.8 \times 10^{15} / [\text{H}]) + R\}, \quad (12)$$

where [H] and [CH₃] are the concentrations (in cm⁻³) at the growing diamond surface, and R is the fraction of radical sites.^{6,7} Typical calculated values of [H], [CH₃], and R under base conditions are ~2 × 10¹⁵ cm⁻³, ~10¹⁴ cm⁻³, and ~0.083, respectively. Contributions to the overall growth rate from other CH_x (x=0–2) species, calculated using the formula G_{CH₃} = 3.9 × 10⁻¹⁴ T_s^{0.5} [CH_x] R (from Refs. 6–8), are predicted to be ~1.4% under the present base conditions.

2D model calculations have been started from a chosen set of initial conditions (e.g., with the chosen feed gas mixture distributed throughout the whole reactor and with low concentrations of charged species in the plasma volume), using standard boundary conditions and the experimental reactor parameters (v_z=0 and v_r=0 at the solid surfaces, a temperature T_{wall}=300 K at the water cooled chamber walls, substrate temperature T_s=973 K, and flow rates F(CH₄)=0–25 SCCM (SCCM denotes cubic centimeters per minute at STP), F(Ar)=40 SCCM, and F(H₂)=[525–F(CH₄)] SCCM). Conservation equations [Eqs. (1)–(5)], together with thermal and caloric equations of state, are solved numerically using the control volume method for an explicit finite difference scheme on a straggle grid.³⁹ Near steady-state species distributions are attained after integrating for physical times t_{phys} > 1 s, though the mole fractions of some stable species (e.g., C₂H₂ and CH₄) are still evolving slowly, mainly in cold regions. The estimated time t_r for gas replacement in the reactor volume V at the base pressure p = 150 Torr is given by t_r = V / {F[SCCM]760 / (60 × 150)} ~ 10 s, indicating that t_r ≫ t_{phys}. Further indirect support for this deduced inequality is provided by the calculated flow velocities (on the order of a few cm s⁻¹ to tens of cm s⁻¹) which are too slow to be important. This analysis confirms

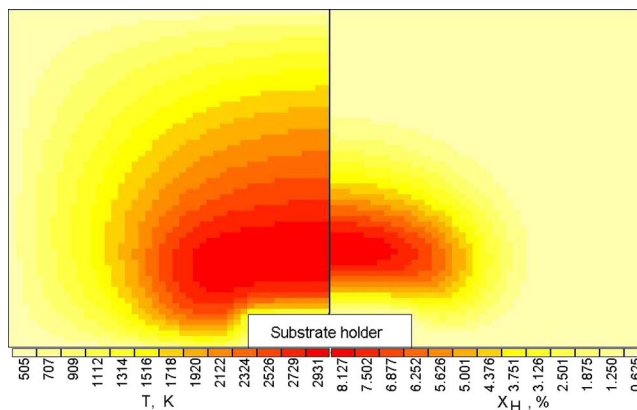


FIG. 1. (Color online) 2D (r, z) plots of the calculated (left) gas temperature T in Kelvin and (right) H atom mole fraction expressed as a percentage, for substrate holder diameter $d_{\text{sh}}=3$ cm and input power $P=1.5$ kW. From the edge of the chamber to the center the color scale increases in 13 equal intervals (left) from 303–505 to 2729–2931 K and (right) from 0%–0.625% to 7.502%–8.127%.

that diffusion and thermal diffusion are the dominant processes of species transfer within the reactor volume.

The 2D model and calculation procedures described above yield spatial distributions of the gas temperature T , the flow field, and the number densities and production/loss rates of all species. In Sec. III we discuss the main plasma-chemical and transport processes and the distributions of T and of species concentrations that are established as a result of these processes.

III. 2D MODELING OF THE FUNDAMENTAL MW PECVD REACTOR PROCESSES

Serial calculations for different reactor and model parameters have been carried out and the results compared with experimental measurements [using cavity ring down spectroscopy (CRDS) that is fully described elsewhere¹⁸] in order to optimize the external model parameters. Effects arising from variation of the many different reactor parameters are illustrated and discussed in the companion papers.^{17–19} Here we present calculated results for base conditions [gas pressure $p=150$ Torr; input power $P=1.5$ kW; feed gas flow rates $F(\text{CH}_4)=25$ SCCM, $F(\text{Ar})=40$ SCCM, and $F(\text{H}_2)=500$ SCCM; substrate temperature $T_s=973$ K; substrate holder diameter $d_s=3$ cm; and a model reactor chamber of diameter $d_r=12$ cm and height $h=6$ cm]. Additional results are presented for a lower input carbon fraction, $F(\text{CH}_4)=5$ SCCM. Figure 1 shows 2D (r, z) false color plots depicting the gas temperature T and atomic hydrogen mole fraction X_{H} distributions within the reactor chamber under base conditions, while Fig. 2 shows the calculated electron and H($n=2$) number density distributions. All of these results were calculated with the following external parameters: cylindrical plasma bulk with radius $r_{\text{pl}} \sim 2.9$ cm and height $0 < z < h_{\text{pl}}=1.4$ cm and electron temperature $T_e \sim 1.28$ eV. The absorbed power density within this plasma volume declines with increasing distance z from the substrate, from ~47 W cm⁻³ at $z \sim 2$ mm above the substrate center to ~30 W cm⁻³ in the center of the hot region at $z \sim 10$ mm.

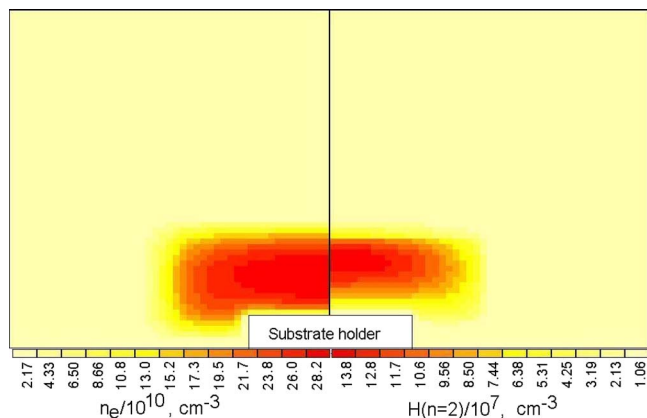


FIG. 2. (Color online) 2D (r, z) plots of the calculated (left) electron and (right) $H(n=2)$ number densities (in cm^{-3}) for base conditions. From the edge of the chamber to the center the color scale increases in 13 equal intervals.

A. Plasma-chemical mechanism

The most important plasma-chemical reactions that determine the power density profiles, as well as the maximum electron densities $n_e \sim 3 \times 10^{11} \text{ cm}^{-3}$ and gas temperature $T \sim 2930 \text{ K}$, are listed in Table I for the center of the plasma region ($r=0$, $z=10.5 \text{ mm}$). As can be seen, $\sim 66\%$ of the input power is partitioned into vibrational excitation and $\sim 27\%$ into rotational excitation of H_2 , and $\sim 5\%$ is lost in elastic collisions of electrons with H_2 . About 1.6% of the absorbed power is consumed in dissociating H_2 molecules following excitation to triplet states.²⁷ The remainder goes into excitation and ionization of various gas species.

As Table I shows, a significant part of the e-V and e-R excitation energy (reactions 1–3) is dissipated as gas heating via R-T and vibrational-translational relaxation [e.g., V-T relaxation of $\text{H}_2(v)$ molecules in collisions with H atoms, reactions 5 and 6]. As a result, the dominant part of the e-V excitation energy is partitioned into H atom kinetic energy—thereby providing a source of translationally excited (“hot”) H atoms which might be detectable if the V-T relaxation rate (reaction 5) is comparable with the (fast) rates of elastic collisions of H atoms with H_2 molecules and other particles. V-T relaxation rate coefficients are predicted to increase sharply with gas temperature [e.g., the probability of V-T relaxation is ~ 0.11 at $T=7500 \text{ K}$ (Ref. 40)], suggesting that V-T relaxation processes could indeed be responsible for the unexpectedly high H atom temperature ($\sim 4750 \text{ K}$) deduced from absorption measurements of the H Balmer- α transition linewidth in the present work¹⁸ and in previous (emission) studies of the same spectral transition in a MW PECVD reactor operating at lower total pressures.⁴¹ V-T relaxation has also been proposed as a possible source of hot H atoms in other lower pressure discharges.⁴² It should be noted that earlier two photon absorption laser induced fluorescence (TALIF) line shape measurements returned H atom translational temperatures in the bulk of a MW discharge plasma in H_2 and CH_4/H_2 mixtures in equilibrium with the measured $\text{H}_2(X)$ rotational temperature throughout the range $10.6 \text{ Torr} \leq p \leq 76 \text{ Torr}$.⁴³

The main ionization processes under our base plasma conditions are electron impact ionization of C_2H_2 , H_2 , and H, and the associative ionization reaction between $\text{H}(n \geq 2)$ atoms and H_2 molecules (reactions 19 and 21 in Table I). H_3^+ is the most abundant ion in a pure Ar/ H_2 mixture but, as Table II shows, it is rapidly usurped by C_2H_2^+ and C_2H_3^+ upon addition of even small amounts of hydrocarbon. The gas processing ensures that C_2H_2 is the most abundant hydrocarbon species in the base plasma. It has a much lower ionization potential ($I_{\text{C}_2\text{H}_2} = 11.4 \text{ eV}$) than H_2 ($I_{\text{H}_2} = 15.6 \text{ eV}$), which ensures that C_2H_2^+ and C_2H_3^+ are the dominant ions under base operating conditions.

We now digress to consider aspects of the hydrocarbon-free Ar/ H_2 plasma. The prevalent ionization processes in this environment are considered to be electron impact ionization of H atoms and of H_2 , and associative ionization reactions 19 and 21 in Table I. Penning ionization involving excited argon atoms and the associative ionization involving $\text{H}(n=2)$ and Ar atoms (Table I, reaction 20) became increasingly important with increasing argon mole fraction. In contrast to the present work, Hassouni *et al.*^{11,30} identified the associative ionization $\text{H}(n > 1) + \text{H}_2 \rightarrow \text{H}_3^+ + e$ as the most important ionization channel in their modeling of Ar/ H_2 and H/C/Ar plasmas, by virtue of the large value assumed for this reaction rate coefficient. Use of the expression $k_{\text{ai}}(\text{cm}^3 \text{ s}^{-1}) = 2.8 \times 10^{-11} T^{0.5}$ implies a value of $1.5 \times 10^{-9} \text{ cm}^3 \text{ s}^{-1}$ at $T = 2900 \text{ K}$, which is much higher than the $k_{\text{ai}} = 1.66 \times 10^{-11} \text{ cm}^3 \text{ s}^{-1}$ value adopted in the present work. The value of this rate coefficient k_{ai} and the products of the quenching of $\text{H}(n > 1)$ by H_2 are both a subject of ongoing controversy.^{44,45} We have carried out a series of test calculations assuming different k_{ai} values in the range $1.66 \times 10^{-11} \text{ cm}^3 \text{ s}^{-1} < k_{\text{ai}} < 3.65 \times 10^{-10} \text{ cm}^3 \text{ s}^{-1}$, and been unable to reproduce our experimental measurements if $k_{\text{ai}} \geq 5 \times 10^{-11} \text{ cm}^3 \text{ s}^{-1}$. Analysis of the balance equations for the electron and $\text{H}(n=2)$ atom number densities in a low-pressure hydrogen dc discharge⁴² also shows that a value $k_{\text{ai}} \geq 5 \times 10^{-11} \text{ cm}^3 \text{ s}^{-1}$ is incompatible with the experimental data for these species. Adopting this upper limit value ($k_{\text{ai}} \sim 5 \times 10^{-11} \text{ cm}^3 \text{ s}^{-1}$), we find it necessary to introduce a simultaneous expansion of the plasma volume ($r_{\text{pl}} = 3 \text{ cm}$) and a reduction in the Lyman- α decay rate (to $A \sim 1.5 \times 10^8 \text{ s}^{-1}$) in order to preserve the maximal gas temperature ($T \sim 2930 \text{ K}$) and match the CH, $\text{C}_2(a)$, and $\text{H}(n=2)$ column densities measured (by CRDS) under base conditions. Such a reduction in A [by a factor of ~ 3 , relative to that for free photon escape ($A = 4.7 \times 10^8 \text{ s}^{-1}$)] would appear reasonable, given the probability of Lyman- α photon reabsorption by $\text{H}(n=1)$ atoms.²⁶ Use of the value $A = 3 \times 10^8 \text{ s}^{-1}$ in our serial calculations with $k_{\text{ai}} = 1.66 \times 10^{-11} \text{ cm}^3 \text{ s}^{-1}$ currently provides the best correlation between the calculated and measured $\text{H}(n=2)$ column densities.

As Table II shows, the dominant ions under our base conditions are C_2H_2^+ and C_2H_3^+ (and H_3^+ in a hydrocarbon-free Ar/ H_2 mixture). The present modeling does not include allowance for any possible conversion to more complex ions (e.g., H_5^+). Such conversions would change e-ion recombination rates and affect the plasma density, but are not expected to introduce any fundamental changes to the results

TABLE I. Absorbed power fractions and the rates and rate coefficients of the important plasma-chemical reactions at the hot region center ($r=0$, $z=10.5$ mm).

N	Rotational and vibrational excitation/relaxation, elastic collisions, V-T relaxation	Reaction rates R ($\text{cm}^{-3} \text{s}^{-1}$)	Rate coefficients, k	Fraction from total power density
			(in s^{-1} for radiation reactions and $\text{cm}^{-3} \text{s}^{-1}$ for all other reactions) ($T_e=1.28$ eV)	$\sim 30 \text{ W cm}^{-3}$ (%)
1	$\text{H}_2(v=0)+e \rightarrow \text{H}_2(v=1)+e$	2.39×10^{20}	2.28×10^{-9}	82.96
2	$\text{H}_2(v=1)+e \rightarrow \text{H}_2(v=0)+e$	4.90×10^{19}	3.60×10^{-9}	-17.02
3	$\text{H}_2(J)+e \leftrightarrow \text{H}_2(J+2)+e$	7.50×10^{20}	6.32×10^{-9}	26.71
4	$\text{H}_2+e \leftrightarrow \text{H}_2+e$, elastic	1.41×10^{22}	1.19×10^{-7}	5.14
5	$\text{H}_2(v=1)+\text{H} \rightarrow \text{H}_2(v=0)+\text{H}$	1.359×10^{23}	6.85×10^{-11}	
6	$\text{H}_2(v=0)+\text{H} \rightarrow \text{H}_2(v=1)+\text{H}$	1.357×10^{23}	8.87×10^{-12}	
Dissociation				
7	$\text{H}_2+\text{H}_2 \rightarrow \text{H}+\text{H}+\text{H}_2$	1.57×10^{19}	8.13×10^{-17}	
8	$\text{H}_2+e \rightarrow \text{H}+\text{H}+e$	6.02×10^{17}	5.08×10^{-12}	1.62
9	$\text{CH}_4+e \rightarrow \text{CH}_3+\text{H}+e$	8.04×10^{13}	1.35×10^{-11}	
10	$\text{C}_2\text{H}_2+e \rightarrow \text{C}_2\text{H}+\text{H}+e$	2.70×10^{16}	3.56×10^{-11}	0.09
11	$\text{C}_2\text{H}+e \rightarrow \text{C}_2+\text{H}+e$	3.12×10^{14}	3.56×10^{-11}	
12	$\text{CH}_4+e \rightarrow \text{CH}_3+\text{H}+e$	1.20×10^{14}	1.35×10^{-11}	
Ionization				
13	$\text{Ar}+e \rightarrow \text{Ar}^++e+e$	7.11×10^{12}	1.99×10^{-15}	
14	$\text{Ar}^++e \rightarrow \text{Ar}^++e+e$	1.10×10^{10}	4.03×10^{-10}	
15	$\text{H}_2^++e \rightarrow \text{H}_2^++e+e$	1.82×10^{11}	3.99×10^{-10}	
16	$\text{H}+e \rightarrow \text{H}^++e+e$	1.60×10^{14}	1.51×10^{-14}	0.001
17	$\text{H}_2+e \rightarrow \text{H}_2^++e+e$	2.12×10^{14}	1.79×10^{-15}	0.002
18	$\text{C}_2\text{H}_2+e \rightarrow \text{C}_2\text{H}_2^++e+e$	1.09×10^{15}	1.44×10^{-12}	0.008
19	$\text{H}(n=2)+\text{H}_2 \rightarrow \text{H}_3^++e$	1.02×10^{15}	1.66×10^{-11}	
20	$\text{H}(n=2)+\text{Ar} \rightarrow \text{ArH}^++e$	3.07×10^{13}	1.66×10^{-11}	
21	$\text{H}(n=3)+\text{H}_2 \rightarrow \text{H}_3^++e$	5.56×10^{13}	1.66×10^{-11}	
22	$\text{Ar}^++\text{C}_2\text{H}_2 \rightarrow \text{Ar}+\text{C}_2\text{H}_2^++e$	9.44×10^{12}	3.32×10^{-11}	
23	$\text{H}_2^++\text{C}_2\text{H}_2 \rightarrow \text{H}_2+\text{C}_2\text{H}_2^++e$	3.95×10^{13}	8.30×10^{-12}	
Recombination				
24	$\text{H}_3^++e \rightarrow \text{H}_2+\text{H}(n=2)$	9.74×10^{11}	1.33×10^{-8}	
25	$\text{C}_2\text{H}_2^++e \rightarrow \text{C}_2\text{H}+\text{H}$	9.84×10^{14}	2.95×10^{-8}	
26	$\text{C}_2\text{H}_3^++e \rightarrow \text{C}_2\text{H}_2+\text{H}$	1.16×10^{15}	2.95×10^{-8}	
Excitation/deexcitation				
27	$\text{H}_2+e \rightarrow \text{H}_2^++e$	3.40×10^{16}	2.73×10^{-13}	0.22
28	$\text{Ar}+e \rightarrow e+\text{Ar}^*$	8.03×10^{14}	2.25×10^{-13}	0.0053
29	$\text{Ar}+e \rightarrow e+\text{Ar}^{**}$	5.59×10^{14}	1.57×10^{-13}	0.0038
30	$\text{Ar}^++\text{H} \rightarrow \text{H}(n=2)+\text{Ar}$	7.92×10^{14}	1.99×10^{-10}	
31	$\text{Ar}^{**}+\text{H} \rightarrow \text{H}(n=2)+\text{Ar}$	2.45×10^{14}	1.99×10^{-10}	
32	$\text{H}(n=2)+e \rightarrow \text{H}(n=3)+e$	3.63×10^{11}	9.64×10^{-9}	
33	$\text{H}(n=3)+e \rightarrow \text{H}(n=2)+e$	1.03×10^{11}	5.01×10^{-8}	
34	$\text{H}+e \rightarrow \text{H}(n=2)+e$	4.25×10^{16}	4.01×10^{-12}	0.245
35	$\text{H}(n=2)+e \rightarrow \text{H}+e$	7.37×10^{11}	1.96×10^{-8}	
36	$\text{H}+e \rightarrow \text{H}(n=3)+e$	8.67×10^{14}	8.17×10^{-14}	0.0055
37	$\text{H}(n=2)+\text{H}_2 \rightarrow \text{H}+\text{H}+\text{H}$	1.02×10^{15}	1.66×10^{-11}	
38	$\text{H}(n=3)+\text{H}_2 \rightarrow \text{H}+\text{H}+\text{H}$	5.56×10^{13}	1.66×10^{-11}	
Radiation				
39	$\text{H}(n=3) \rightarrow \text{H}(n=2)+h\nu$	3.35×10^{14}	4.40×10^7	
40	$\text{H}(n=2) \rightarrow \text{H}(n=1)+h\nu$	4.18×10^{16}	3.00×10^8	
41	$\text{H}(n=3) \rightarrow \text{H}(n=1)+h\nu$	4.19×10^{14}	5.50×10^7	
42	$\text{H}_2^* \rightarrow \text{H}_2+h\nu$	3.39×10^{16}	2.00×10^7	
43	$\text{Ar}^{**} \rightarrow \text{Ar}+h\nu$	3.13×10^{14}	1.00×10^7	
Ion chemistry				
44	$\text{Ar}^++\text{H}_2 \rightarrow \text{ArH}^++\text{H}$	6.36×10^{12}	1.20×10^{-9}	
45	$\text{Ar}^++\text{H}_2 \rightarrow \text{H}_2^++\text{Ar}$	7.46×10^{11}	1.40×10^{-10}	

TABLE I. (Continued.)

N	Rotational and vibrational excitation/relaxation, elastic collisions, V-T relaxation	Reaction rates R ($\text{cm}^{-3} \text{s}^{-1}$)	Rate coefficients, k	
			(in s^{-1} for radiation reactions and $\text{cm}^{-3} \text{s}^{-1}$ for all other reactions) ($T_e = 1.28 \text{ eV}$)	Fraction from total power density $\sim 30 \text{ W cm}^{-3}$ (%)
46	$\text{Ar}^+ + \text{C}_2\text{H}_2 \rightarrow \text{C}_2\text{H}_2^+ + \text{Ar}$	1.36×10^{10}	4.00×10^{-10}	
47	$\text{ArH}^+ + \text{H}_2 \rightarrow \text{H}_3^+ + \text{Ar}$	3.72×10^{14}	4.98×10^{-10}	
48	$\text{H}^+ + \text{C}_2\text{H}_2 \rightarrow \text{C}_2\text{H}_2^+ + \text{H}$	1.60×10^{14}	2.00×10^{-9}	
49	$\text{H}_2^+ + \text{H}_2 \rightarrow \text{H}_3^+ + \text{H}$	2.03×10^{14}	1.99×10^{-9}	
50	$\text{H}_2^+ + \text{Ar} \rightarrow \text{ArH}^+ + \text{H}$	3.69×10^{12}	1.20×10^{-9}	
51	$\text{H}_3^+ + \text{C}_2\text{H}_2 \rightarrow \text{H}_2 + \text{C}_2\text{H}_2^+$	3.14×10^{12}	4.82×10^{-9}	
52	$\text{H}_2^+ + \text{C}_2\text{H}_2 \rightarrow \text{C}_2\text{H}_3^+ + \text{H}$	3.14×10^{12}	4.82×10^{-9}	
53	$\text{H}_3^+ + \text{Ar} \rightarrow \text{ArH}^+ + \text{H}_2$	3.30×10^{14}	9.19×10^{-11}	
54	$\text{H}_3^+ + \text{C}_2\text{H}_2 \rightarrow \text{H}_2 + \text{C}_2\text{H}_3^+$	1.48×10^{15}	1.94×10^{-9}	

reported here. We also highlight a recurring problem with applying reported e-ion recombination coefficients k_{re} to hot plasma conditions: most measurements of k_{re} have been carried out at (or near) room temperature, and thus will not capture features that are specific to higher temperature plasmas. For example, k_{re} of H_3^+ ions shows a strong vibrational (v) state dependence.⁴⁶ We can anticipate that the $\text{H}_3^+(v)$ state distribution will be near Boltzmann in our hot dense gas mixtures, under which circumstances we might expect most $\text{H}_3^+(v) + e$ recombinations to involve levels with $v = 1, 2$.

Thermal dissociation (reaction 7 in Table I) exceeds electron impact dissociation of H_2 molecules (reaction 8 in Table I) by more than an order of magnitude under our base conditions. However, the relative contribution of plasma sources of dissociation becomes more and more significant with increasing argon dilution. Furthermore, as shown in our previous simulations of UNCD deposition in MW PECVD reactors, this source prevails at high X_{Ar} and can provide an extremely high degree of dissociation (e.g., $X_{\text{H}} \sim 2.6\% \gg X_{\text{H}_2} \sim 0.16\%$).⁶

B. Hydrocarbon conversion, plasma glow region, and diamond deposition processes

The present simulations allow us to paint a uniquely complete and coherent picture of the complex hydrocarbon interconversion processes occurring throughout the entire reactor volume. Figure 3 shows a 2D false color picture of the methane and acetylene mole fraction distributions under base conditions. Three regions are indicated on the right panel of this figure: the central, hot plasma region A, and two hemispherical shells B and C characterized by different average gas temperatures and H atom mole fractions. As discussed in detail elsewhere,¹⁷ the input CH_4 is converted into C_2H_2 in region B, at gas temperatures $1400 \text{ K} < T < 2200 \text{ K}$. This conversion involves significant consumption of H atoms (~ 4 H atoms per $2\text{CH}_4 \rightarrow \text{C}_2\text{H}_2$ conversion). The reverse $\text{C}_2\text{H}_2 \rightarrow \text{CH}_4$ conversion occurs in region C, at gas temperatures $500 \text{ K} < T < 1400 \text{ K}$. This conversion involves no net consumption of H atoms, though the H atoms play a crucial role (essentially acting as a catalyst) for this multistep conversion.

The central hot region, A, is characterized by near-equilibrium distributions in both the C_1H_x ($x=0-4$) and

TABLE II. Gas temperatures T (in K) and species concentrations (in cm^{-3}) just above the center of the substrate ($r=0$, $z=0.5 \text{ mm}$) and in the center of the hot region ($r=0$, $z=10.5 \text{ mm}$) under base [$F(\text{CH}_4)=25 \text{ SCCM}$] and reduced [$F(\text{CH}_4)=5 \text{ SCCM}$] input hydrocarbon flow rates.

	$F(\text{CH}_4)=25 \text{ SCCM}$		$F(\text{CH}_4)=5 \text{ SCCM}$	
	z (mm)	T (K)	z (mm)	T (K)
$X_{\text{CH}_4}^0$	0.044	0.044	0.0088	0.0088
z (mm)	0.5	10.5	0.5	10.5
T (K)	1305	2926	1273	2926
H	8.19×10^{15}	3.93×10^{16}	8.37×10^{15}	3.68×10^{16}
CH_4	1.02×10^{15}	2.21×10^{13}	5.60×10^{14}	1.50×10^{13}
CH_3	1.13×10^{14}	3.29×10^{13}	5.53×10^{13}	2.10×10^{13}
CH_2	4.62×10^{11}	5.08×10^{12}	2.38×10^{11}	3.03×10^{12}
$\text{CH}_2(s)$	1.13×10^{10}	5.93×10^{11}	4.98×10^9	3.53×10^{11}
CH	1.73×10^{10}	1.23×10^{12}	9.40×10^9	6.84×10^{11}
C	5.09×10^{10}	1.73×10^{12}	5.75×10^{10}	9.00×10^{11}
$\text{C}_2(a)$	6.26×10^7	8.28×10^{11}	3.13×10^7	2.33×10^{11}
$\text{C}_2(X)$	1.49×10^7	1.85×10^{11}	3.72×10^6	4.53×10^{10}
C_2H	3.06×10^{10}	3.25×10^{13}	6.34×10^9	8.45×10^{12}
C_2H_2	1.05×10^{16}	2.81×10^{15}	2.89×10^{15}	7.82×10^{14}
C_2H_3	1.94×10^{13}	8.34×10^{11}	6.06×10^{12}	2.40×10^{11}
C_2H_4	4.84×10^{14}	6.10×10^{11}	1.55×10^{14}	1.87×10^{11}
C_2H_5	2.67×10^{11}	4.20×10^8	9.41×10^{10}	1.79×10^8
C_2H_6	1.01×10^{12}	2.96×10^7	3.31×10^{11}	1.30×10^7
C_3	1.28×10^{13}	1.21×10^{12}	3.88×10^{12}	1.75×10^{11}
C_3H	1.89×10^{11}	3.73×10^{10}	4.83×10^{10}	5.78×10^9
C_3H_2	2.12×10^{14}	4.46×10^{12}	5.46×10^{13}	7.40×10^{11}
C_4	2.91×10^5	1.31×10^9	3.38×10^4	9.02×10^7
C_4H	1.03×10^8	4.25×10^{10}	1.10×10^7	3.12×10^9
C_4H_2	1.93×10^{13}	3.34×10^{12}	2.50×10^{12}	2.59×10^{11}
$\text{H}(n=2)$	4.84×10^6	1.39×10^8	5.49×10^6	1.65×10^8
$\text{H}(n=3)$	1.68×10^5	7.62×10^6	1.83×10^5	9.41×10^6
$\text{H}_2(v>0)$	1.24×10^{16}	5.05×10^{16}	1.12×10^{16}	5.06×10^{16}
H_2^*	5.26×10^8	1.69×10^9	5.69×10^8	2.21×10^9
Ar^*	1.71×10^8	1.01×10^8	2.67×10^8	1.80×10^8
Ar^{**}	1.98×10^7	3.13×10^7	2.80×10^7	5.36×10^7
e	9.65×10^{10}	2.70×10^{11}	7.12×10^{10}	2.54×10^{11}
C_2H_2^+	6.04×10^{10}	1.23×10^{11}	2.19×10^{10}	4.98×10^{10}
C_2H_3^+	3.61×10^{10}	1.46×10^{11}	4.92×10^{10}	2.03×10^{11}
H_3^+	7.06×10^6	2.71×10^8	3.19×10^7	1.21×10^9
H_2^+	2.13×10^4	2.32×10^5	2.60×10^4	3.41×10^5
ArH^+	1.70×10^4	1.70×10^6	4.26×10^4	8.88×10^6
Ar^+	1.64×10^3	1.21×10^4	2.56×10^3	2.25×10^4
H^+	1.39×10^8	2.85×10^7	7.26×10^5	1.32×10^8
Ar	4.27×10^{16}	1.32×10^{16}	5.64×10^{16}	1.69×10^{16}
$\text{H}_2(v=0)$	1.03×10^{18}	3.89×10^{17}	1.06×10^{18}	3.90×10^{17}

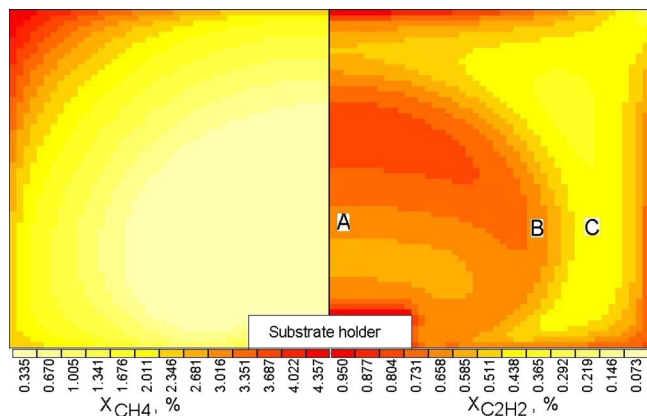


FIG. 3. (Color online) 2D (r,z) plots of the calculated (left) CH_4 and (right) C_2H_2 mole fractions expressed as a percentage, for base conditions. The color scale increases in 13 equal intervals.

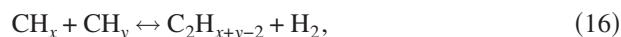
C_2H_y ($y=0-6$) species groups. Fast H-shifting and H recombination/thermal decomposition reactions^{3,17,18} ensure maintenance of the equilibrium within each group, and we can draw the following general guidelines for estimating hydrocarbon species concentrations:

$$[\text{CH}_x] = f1_x(T, H, \text{H}_2)[\text{C}_1], \quad (13)$$

$$[\text{C}_2\text{H}_y] = f2_y(T, H, \text{H}_2)[\text{C}_2], \quad (14)$$

where $[\text{C}_1]$ and $[\text{C}_2]$ are the total concentrations of C_1 and C_2 species, respectively. $f1_x$ and $f2_y$ are the respective partition functions, which mainly depend on the local T and the degree of H_2 dissociation.

The much slower exchange between the groups, e.g., via the reactions



is also in balance. The overall balance lies strongly in favor of the C_2H_y group at the gas temperatures $2000 \text{ K} < T < 3000 \text{ K}$ prevailing in the hot central region, with the result that $>97\%$ of the gas phase carbon in this region is calculated to be in the form of C_2H_2 molecules. Table II lists the calculated species concentrations and T at two distances from the substrate center, $z=0.5 \text{ mm}$ and $z=10.5 \text{ mm}$, and for two input methane flow rates [corresponding to input mole fractions $X_{\text{CH}_4}^0=0.044$ (base conditions) and $X_{\text{CH}_4}^0=0.0088$]. Under base conditions, we determine $f1_4 \sim 0.347$, $f1_3 \sim 0.517$, $f1_2 \sim 0.089$, $f1_1 \sim 0.019$, and $f1_0 \sim 0.027$, $T=2926 \text{ K}$, and $[\text{H}]/[\text{H}_2]=0.09$ in the center of the hot region. From the detailed balance of exchange reactions (15) and (16) above, together with Eq. (13), we can derive the functional dependence $[\text{C}_1] \sim [\text{C}_2]^{0.5}$. In turn, $[\text{C}_2] \approx 0.5b_{\text{TD}}X_{\text{C}_1}^0N$, where $X_{\text{C}_1}^0$ is the carbon fraction in the input gas mixture (i.e., $X_{\text{C}_1}^0=0.044$ for base conditions) and b_{TD} is a factor that describes the reduction in the total carbon balance in hot regions as a result of thermodiffusional transfer.⁴⁷ The calculated value of b_{TD} is ~ 0.3 for the central plasma region ($T \sim 2900 \text{ K}$). Thus, in the hot region (and even close above the substrate—see Table II), we deduce that for CH_x

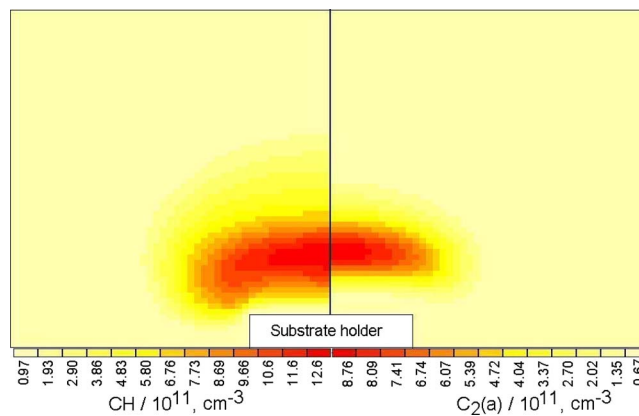


FIG. 4. (Color online) 2D (r,z) plots of the calculated (left) CH and (right) $\text{C}_2(a)$ number densities (in cm^{-3}) for base conditions. From the edge of the chamber to the center the color scale increases in 13 equal intervals.

and C_2H_y concentrations will show the following dependences on input carbon mole fraction:

$$[\text{CH}_x] \propto (X_{\text{C}_1}^0)^{0.5}, \quad (17)$$

$$[\text{C}_2\text{H}_y] \propto X_{\text{C}_1}^0. \quad (18)$$

Further, Table II shows that the following relationship can provide a practical estimate of the CH_3 mole fraction close above the substrate for the present (and similar) MW PECVD reactor conditions:

$$X_{\text{CH}_3} \approx 5 \times 10^{-4} (X_{\text{C}_1}^0)^{0.5}. \quad (19)$$

The respective square root and linear dependences on input carbon mole fraction derived in Eqs. (17) and (18) accord with the measured variations in CH and $\text{C}_2(a)$ column densities.¹⁸ Figure 4 shows the calculated 2D distributions of these two radical species. The CH distribution is somewhat more extensive, but both are clearly localized in the hot central region. Swan band emission, from electronically excited $\text{C}_2(d)$ radicals, is largely responsible for the apparent visible size of the plasma ball in most MW reactors [with lesser contributions from atomic $\text{H}(n>2)$ and from electronically excited CH radicals]. However, comparing the visual size of the plasma region with the spatial distributions of H atoms (Fig. 1), or of CH_3 and CH_2 radicals (Fig. 5), it is clear that the reactive region is much larger than the visibly luminescent plasma region. The calculated profiles of CH_3 , CH_2 , and CH [Figs. 5 and 4 (left)] serve to illustrate the sensitivity of the CH_x group species to the local gas temperature and $[\text{H}]/[\text{H}_2]$ ratio. Higher T and $[\text{H}]/[\text{H}_2]$ ratios shift the equilibrium in favor of CH and C (not shown) as well as C_2 [Fig. 4 (right)] and C_2H (which is not shown but closely mimics that of C_2).

As Fig. 5 shows, the CH_3 number density maximizes around the periphery of the plasma region. Knowledge of the radial profiles of the H atoms and CH_3 radicals above the substrate surface allows prediction of the likely area of diamond deposition, uniformity, and growth rates for the reactor conditions under study. The calculated concentrations of H atoms ($\sim 1.8 \times 10^{15} \text{ cm}^{-3}$) and CH_3 radicals ($\sim 1.1 \times 10^{14} \text{ cm}^{-3}$) are near uniform across the entire top surface

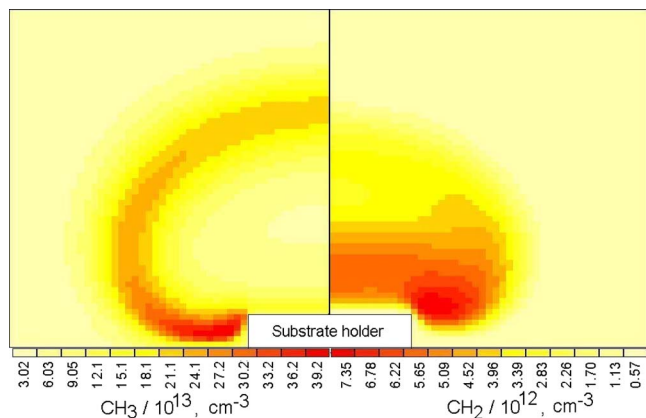


FIG. 5. (Color online) 2D (r,z) plots of the calculated (left) CH_3 and (right) CH_2 number densities (in cm^{-3}) for base conditions. The color scale increases in 13 equal intervals.

of the substrate (i.e., $r \leq 1.5$ cm). Application of Eq. (12) results in predicted growth rates $G \sim 4$ and $\sim 2 \mu\text{m h}^{-1}$ for $X_{\text{CH}_4}^0 = 0.044$ (base conditions) and $X_{\text{CH}_4}^0 = 0.0088$, respectively—values which correlate well with the experimentally observed growth rates ($G \sim 2 \mu\text{m h}^{-1}$ under base conditions). Dependence (17) also implies that the growth rate in the case of growth from CH_3 [or any other CH_x ($x = 0-2$) species] should be proportional to the square root of the initial carbon fraction in the feed gas. Such a dependence upon $G(X_{\text{C1}}^0)$ has been reported in a number of studies,⁴⁸ including the recent data of Li *et al.*⁴⁹ at CH_4 flow rates of up to a few percent. At yet higher ($>5\%$ of the total input) flow rates, G is seen to grow more steeply, but this change is accompanied by obvious changes in morphology (from MCD to NCD).⁶

IV. CONCLUSIONS

The results of the 2D model calculations described herein provide a coherent picture of the basic plasma-chemical and transport processes prevailing in a MW PECVD reactor under conditions appropriate for MCD growth. Identification of the important plasma-chemical reactions and quantification of the channels by which the absorbed MW power is utilized results in the following typical plasma parameters for base reactor conditions: power densities $P \sim 30 \text{ W cm}^{-3}$, electron concentrations $n_e \sim 3 \times 10^{11} \text{ cm}^{-3}$, gas temperatures $T \sim 2900 \text{ K}$, and hydrogen mole fraction $X_{\text{H}} \sim 8\%$. The concentrations of atomic hydrogen, $[\text{H}] \sim 2 \times 10^{15} \text{ cm}^{-3}$, and methyl radicals, $[\text{CH}_3] \sim 10^{14} \text{ cm}^{-3}$, at the substrate surface determine the MCD growth rates $G \sim 2-4 \mu\text{m h}^{-1}$. The reactor volume is visualized in terms of three nested zones, characterized by different gas phase chemistries. The initial activations of CH_4 and C_2H_2 through reaction with H atoms, as well as the thermally driven interconversions between the C_1H_x and C_2H_y groups, occur in regions B and C beyond the hot plasma region A that is visible to the eye. The detailed balances within C_1H_x and C_2H_y groups in the hot region A are maintained by fast H-shifting reactions and by thermal decomposition/recombination reactions. Exchange between the C_1H_x and C_2H_y groups occurs much more slowly (as

discussed more fully elsewhere¹⁷) and shifts in favor of the C_2H_y family at higher temperatures—to the extent that $>97\%$ of the total gas phase carbon in the hot central region is calculated to be present in the form of C_2H_2 .

These findings allow us to propose a simple procedure for estimating the CH_x and C_2H_y concentrations in regions relevant for diamond growth, and for deriving their dependence on input carbon mole fraction: $[\text{CH}_x] \propto (X_{\text{C1}}^0)^{0.5}$ and $[\text{C}_2\text{H}_y] \propto X_{\text{C1}}^0$. For example, the relationship $X_{\text{CH}_3} \approx 5 \times 10^{-4} (X_{\text{C1}}^0)^{0.5}$ can be used to provide a practical estimate of the CH_3 mole fraction above the substrate in the present (and similar) MW PECVD reactor conditions. The derived square root and linear dependences on carbon input mole fraction are supported by the CRDS measurements of CH and $\text{C}_2(a)$ column densities,¹⁸ respectively, and by the growth rate dependence $G \propto (X_{\text{C1}}^0)^{0.5}$ observed experimentally. Systematic tests of the 2D model on a wealth of experimental data, recorded as a function of distance above the substrate surface, and for a wide variety of reactor parameters (e.g., gas pressure, input power, and carbon mole fraction) are described in the companion papers.¹⁷⁻¹⁹

ACKNOWLEDGMENTS

Y.A.M. is grateful to RF Government for Key Science Schools Grant No. 133.2008.2. The Bristol group is grateful to EPSRC for the award of a portfolio grant (LASER); Element Six Ltd. for financial support and the long term loan of a MW reactor that enabled the complementary experimental measurements; the University of Bristol and the Overseas Research Scholarship (ORS) scheme for a postgraduate scholarship (J.M.); and Bristol colleagues K. N. Rosser, Dr. A. Cheesman, Dr. J. A. Smith, Dr. C. M. Western, and Professor A. J. Orr-Ewing, Dr. J. E. Butler (Naval Research Laboratory, Washington), and Professor G. Duxbury (University of Strathclyde) for their many and varied contributions to this project.

¹P. W. May, *Philos. Trans. R. Soc. London, Ser. A* **358**, 473 (2000).

²S. J. Harris, *Appl. Phys. Lett.* **56**, 2298 (1990).

³D. G. Goodwin and J. E. Butler, in *Handbook of Industrial Diamonds and Diamond Films*, edited by M. A. Prelas, G. Popovici, and L. K. Bigelow (Dekker, New York, 1998).

⁴D. Zhou, D. M. Gruen, L. C. Qin, T. G. McCauley, and A. R. Krauss, *J. Appl. Phys.* **84**, 1981 (1998).

⁵P. W. May, J. N. Harvey, J. A. Smith, and Yu. A. Mankelevich, *J. Appl. Phys.* **99**, 104907 (2006).

⁶P. W. May and Yu. A. Mankelevich, *J. Phys. Chem. C* **112**, 12432 (2008).

⁷P. W. May, M. N. R. Ashfold, and Yu. A. Mankelevich, *J. Appl. Phys.* **101**, 053115 (2007).

⁸Yu. A. Mankelevich and P. W. May, *Diamond Relat. Mater.* **17**, 1021 (2008).

⁹G. Bogdan, M. Nesládek, J. D'Haen, J. Maes, V. V. Moshchalkov, K. Haenen, and M. D'Olieslaeger, *Phys. Status Solidi A* **202**, 2066 (2005).

¹⁰S. V. Kostiuik, Yu. A. Mankelevich, A. T. Rakhimov, and N. V. Suetin, *Proceedings of the Fifth International Symposium on Diamond Materials*, edited by J. L. Davidson, W. D. Brown, A. Gicquel, B. V. Spitsyn, and J. C. Angus (Electrochemical Society, Paris, 1997), Vol. 97-32, p. 152.

¹¹K. Hassouni, T. A. Grotjohn, and A. Gicquel, *J. Appl. Phys.* **86**, 134 (1999).

¹²S. V. Kostiuik, Yu. A. Mankelevich, A. T. Rakhimov, and N. V. Suetin, *Moscow, Nauka, Fizmatlit: Proc. of Physics and Technology Inst.* **16**, 38 (2000).

¹³A. M. Gorbachev, V. A. Koldanov, and A. L. Vikharev, *Diamond Relat. Mater.* **10**, 342 (2001).

- ¹⁴H. Yamada, A. Chayahara, and Y. Mokuno, *J. Appl. Phys.* **101**, 063302 (2007).
- ¹⁵G. Lombardi, K. Hassouni, G.-D. Stancu, L. Mechold, J. Ropcke, and A. Gicquel, *J. Appl. Phys.* **98**, 053303 (2005).
- ¹⁶G. Lombardi, K. Hassouni, F. Benedic, F. Mohasseb, J. Ropcke, and A. Gicquel, *J. Appl. Phys.* **96**, 6739 (2004).
- ¹⁷J. Ma, A. Cheesman, M. N. R. Ashfold, K. Hay, S. Wright, N. Langford, G. Duxbury, and Yu. A. Mankelevich, *J. Appl. Phys.* (unpublished).
- ¹⁸J. Ma, J. C. Richley, M. N. R. Ashfold, and Yu. A. Mankelevich, *J. Appl. Phys.* **104**, 103305 (2008).
- ¹⁹J. Ma, M. N. R. Ashfold, and Yu. A. Mankelevich, *J. Appl. Phys.* (in press).
- ²⁰Yu. P. Raizer, *Gas Discharge Physics* (Springer-Verlag, Berlin, 1991).
- ²¹Y. Xu and M. D. Smooke, *J. Comput. Phys.* **104**, 99 (1993).
- ²²B. V. Alekseev and A. M. Grishin, *Physical Gas Dynamics of Reactive Flows* (High School, Moscow, 1985).
- ²³D. S. Dandy and M. E. Coltrin, *J. Mater. Res.* **10**, 1993 (1995).
- ²⁴*Handbook of Physical Data*, edited by I. S. Grigoriev and E. Z. Meiliov (Energoatomizdat, Moscow, 1991).
- ²⁵G. P. Smith, D. M. Golden, M. Frenklach, N. W. Moriarty, B. Eiteneer, M. Goldenberg, C. T. Bowman, R. K. Hanson, C. Song, W. C. Gardiner, Jr., V. V. Lissianski, and Z. Qin, <http://www.me.berkeley.edu/gri-mech>
- ²⁶Yu. A. Mankelevich, A. J. Orr-Ewing, and M. N. R. Ashfold, *J. Appl. Phys.* **102**, 063310 (2007).
- ²⁷A. G. Engelhardt and A. V. Phelps, *Phys. Rev.* **131**, 2115 (1963).
- ²⁸J. H. Kiefer and R. W. Lutz, *J. Chem. Phys.* **44**, 668 (1966).
- ²⁹P. M. Stone, Y. K. Kim, and J. P. Desclaux, *J. Res. Natl. Inst. Stand. Technol.* **107**, 327 (2002).
- ³⁰K. Hassouni, A. Gicquel, M. Capitelli, and J. Loureiro, *Plasma Sources Sci. Technol.* **8**, 494 (1999).
- ³¹G. M. Petrov and Ts. Petrova, *Plasma Chem. Plasma Process.* **22**, 573 (2002).
- ³²J.-S. Yoon, M.-Y. Song, J.-M. Han, S. H. Hwang, W.-S. Chang, B. Lee, and Y. Itikawa, *J. Phys. Chem. Ref. Data* **37**, 913 (2008).
- ³³F. Linder and H. Schmidt, *Z. Naturforsch. A* **26A**, 1603 (1971).
- ³⁴Y.-K. Kim, K. K. Irikura, M. E. Rudd *et al.*, NIST: Electron-Impact Cross-Section Database, http://physics.nist.gov/PhysRefData/Ionization/EII_table.html
- ³⁵E. W. McDaniel and M. R. Flannery, U.S. Army Missile Research and Development Command, Technical Report H-78-1, 1978.
- ³⁶Yu. A. Mankelevich, A. T. Rakhimov, N. V. Suetin, and S. V. Kostiuik, *Diamond Relat. Mater.* **5**, 964 (1996).
- ³⁷B. J. Wood and H. Wise, *J. Phys. Chem.* **65**, 1976 (1961).
- ³⁸L. V. Krasnoperov, L. J. Kalinovski, H. N. Chu, and D. Gutman, *J. Phys. Chem.* **97**, 11787 (1993).
- ³⁹O. M. Belotserkovskii, *Numerical Simulation in Continuum Medium Mechanics* (Nauka, Moscow, 1984).
- ⁴⁰C. Gorse, M. Capitelli, M. Bacal, J. Bretagne, and A. Lagana, *Chem. Phys.* **117**, 177 (1987).
- ⁴¹T. Lang, J. Stiegler, Y. von Kaenel, and E. Blank, *Diamond Relat. Mater.* **5**, 1171 (1996).
- ⁴²J. Amorim, J. Loureiro, G. Baravian, and M. Touzeau, *J. Appl. Phys.* **82**, 2795 (1997).
- ⁴³A. Gicquel, K. Hassouni, Y. Breton, M. Chenevier, and J. C. Cubertafon, *Diamond Relat. Mater.* **5**, 366 (1996).
- ⁴⁴M. Glass-Maujean, *Phys. Rev. Lett.* **62**, 144 (1989).
- ⁴⁵N. Terazawa, M. Ukai, N. Kouchi, K. Kameta, Y. Hatano, and K. Tanaka, *J. Chem. Phys.* **99**, 1637 (1993).
- ⁴⁶H. Hus, F. Youssif, A. Sen, and J. B. A. Mitchell, *Phys. Rev. A* **38**, 658 (1988).
- ⁴⁷M. N. R. Ashfold, P. W. May, J. R. Petherbridge, K. N. Rosser, J. A. Smith, Yu. A. Mankelevich, and N. V. Suetin, *Phys. Chem. Chem. Phys.* **3**, 3471 (2001).
- ⁴⁸H. Sternschulte, T. Bauer, M. Schreck, and B. Stritzker, *Diamond Relat. Mater.* **15**, 542 (2006), and references therein.
- ⁴⁹X. L. Li, J. Perkins, R. Collazo, R. J. Nemanich, and Z. Sitar, *Diamond Relat. Mater.* **15**, 1784 (2006).